Research Square

Preprints are preliminary reports that have not undergone peer review.
They should not be considered conclusive, used to inform clinical practice,
or referenced by the media as validated information.

Multi-objective Optimization in Sports Equipment Design Using Expected Hypervolume Improvement: A Discus and a Race Car Rear Wing

Kazuya Seo

seo@cc.kogakuin.ac.jp

Kogakuin University

Yuki Fujinami

Kogakuin University

Ryoto Nakamura

Kogakuin University

Kotaro Ishikawa

Kogakuin University

Research Article

Keywords: sports equipment design, expected hypervolume improvement, discus, multi-objective optimization, race car rear wing

Posted Date: July 8th, 2026

DOI: https://doi.org/10.21203/rs.3.rs-10211523/v1

License: This work is licensed under a Creative Commons Attribution 4.0 International License.
Read Full License

Additional Declarations: Competing interest reported. Conflict of interest Kazuya Seo serves on the Editorial Board of Sports Engineering. To avoid any potential conflict of interest, Kazuya Seo was not involved in the peer review or editorial decision-making process for this manuscript.

Multi-objective Optimization in Sports Equipment Design Using Expected Hypervolume Improvement: A Discus and a Race Car Rear Wing

Kazuya Seo[1*], Yuki Fujinami[1], Ryoto Nakamura[1] and Kotaro Ishikawa[1]

[1*]Department of Mechanical Engineering, Kogakuin University, 1-24-2 Nishi Shinjuku, Shinjuku, 163-8677, Tokyo, Japan.

*Corresponding author. E-mail: seo@cc.kogakuin.ac.jp;

Contributing author: am25007@ns.kogakuin.ac.jp

Abstract.
This paper presents the application of expected hypervolume improvement (EHVI) to the design of sports equipment involving multiple objective functions. The results demonstrate that EHVI can identify Pareto-optimal solutions and key design variables. However, the EHVI-selected solutions tend to cluster near the center of the objective space, suggesting limited ability to identify extreme Pareto-optimal solutions and to ensure sufficient diversity among the selected solutions. In the discus case, the radius of the metal rim was found to be a key design parameter for increasing flight distance because of its role in delaying stall. In the race car rear-wing case, the angle of attack was identified as the primary design parameter for reducing drag and increasing downforce, while wing area served as a secondary parameter that compensates for the effect of the angle of attack.
Keywords: sports equipment design, expected hypervolume improvement, discus, multi-objective optimization, race car rear wing

1 Introduction

In our previous study [1], an Expected Improvement (EI) criterion was proposed for sports equipment design. In that study, only a single objective function, namely the maximum flight distance of a men's discus, was considered. However, sports equipment design often involves multiple competing objectives, such as aerodynamic performance, structural strength, and cost. These problems result in a set of Pareto-optimal solutions due to inherent trade-offs among the objectives. Because evaluations frequently rely on computationally expensive simulations—particularly for aerodynamic equipment in throwing events and motorsports—reducing the number of evaluations while effectively identifying promising designs is a critical challenge in sports engineering.

This study proposes the use of Expected Hypervolume Improvement (EHVI) [2] as a criterion for efficiently selecting design variables in multi-objective sports equipment optimization. To demonstrate its applicability, we present two aerodynamic case studies: a men's discus and a racing car rear wing. These examples illustrate how the proposed framework can support systematic, performance-oriented sports equipment design across diverse sporting contexts.

In this paper, the performance of EHVI is first demonstrated using a test problem, the welded beam design problem. Subsequently, two examples of multi-objective sports equipment optimization—a race car rear wing and a discus—are presented and discussed.

2 Methods

2.1 Overview of this study

The flowchart in Figure 1 provides an overview of this study. Methods are enclosed in ellipses, while outputs are enclosed in rectangles.

The first phase, labeled as Steps 1 and 2, is the preparation of the initial sets of design variables,

$\boldsymbol{x}$, using Latin Hypercube Sampling (LHS) [3]. Ideally, the number of initial design sets is more than $5d$, where d is the number of design variables. Next, in Step 3, CAD modeling is performed to create sports equipment, such as a discus or a race car rear wing, for all initial design sets, as illustrated in Step 4. For the discus, four design variables are considered, whereas for the race car rear wing, seven design variables are used.

Next, CFD (Computational Fluid Dynamics) or EFD (Experimental Fluid Dynamics) analysis is carried out in Step 5 to determine the aerodynamic coefficients, as shown in Step 6. In the discus case, the flight trajectory is simulated in Step 7, and the flight distance and robustness are evaluated in Step 8. The objective functions for the discus are the flight distance and robustness [4]. If the number of samples is sufficient, as checked in Step 9, the process exits the loop and proceeds to post-processing tasks, such as generating Self-Organizing Maps (SOMs). If not, the procedure continues within the loop. For the race car rear wing case, since the aerodynamic coefficients themselves serve as the objective functions, Steps 7 and 8 are omitted.

The next stage, Step 10, is the normalization of the objective functions and design variables. Normalization is required to compare objective functions of different orders of magnitude or different concepts, which often have different units. Step 11 involves constructing a response surface using Gaussian Process Regression (GPR), which provides the predicted mean and variance corresponding to a given input $\boldsymbol{x}$, as shown in Step 12. In this study, the index of promising design sets is defined as the Expected Hypervolume Improvement (EHVI), which serves as the acquisition function a in Step 13. Step 14 involves identifying the most promising design variable set $\boldsymbol{x}^*$, as described in Step 15. To accomplish this, the acquisition function a is maximized using a genetic algorithm (GA) [5]. Once a new promising design set is found, the process returns to Step 3 for CAD modeling and repeats until the stopping criteria in Step 9 are satisfied.

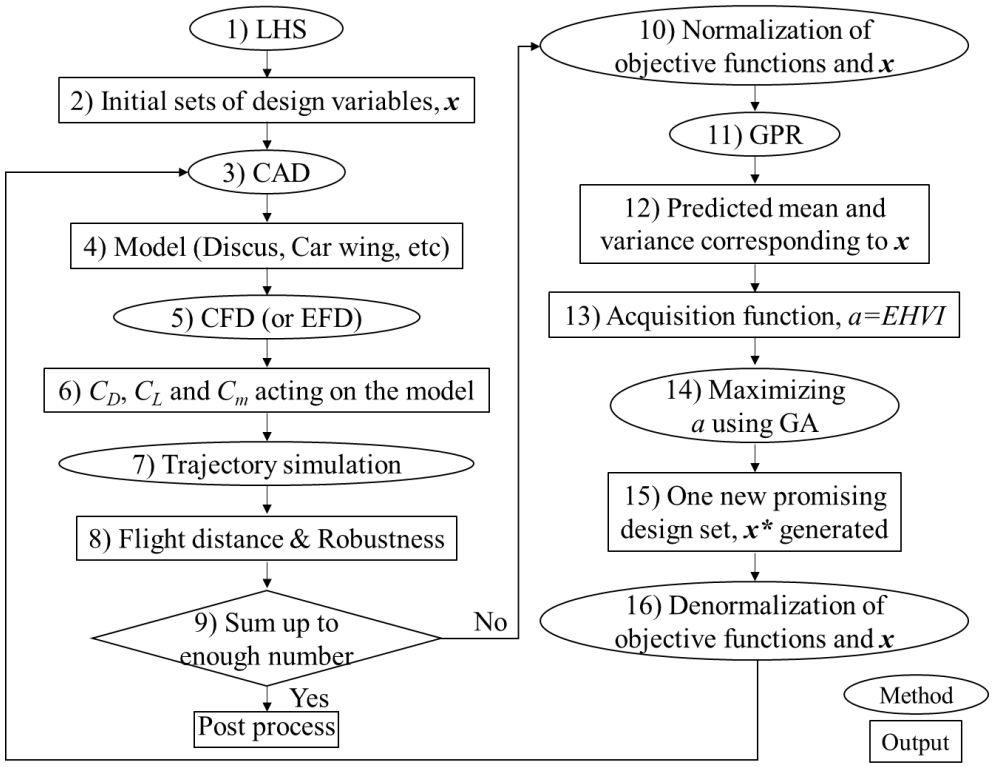
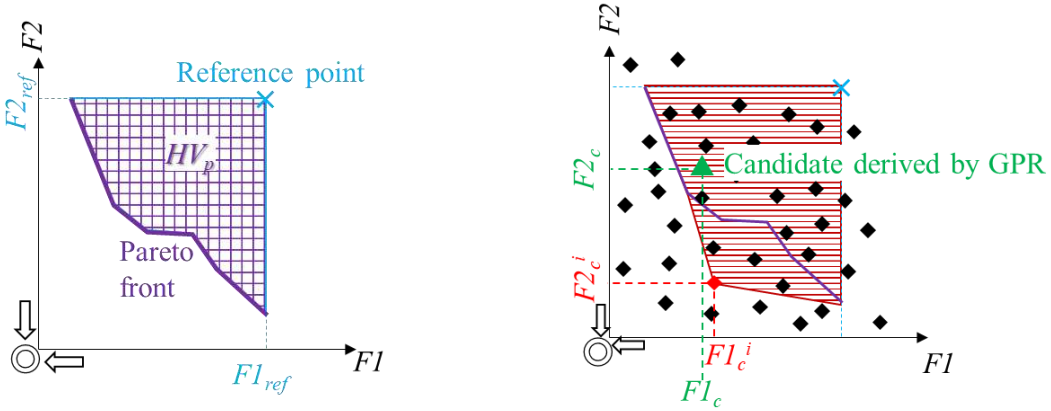


Fig. 1 Overview of this study. Flowchart of the multi-objective optimization process in sports equipment design using Expected Hypervolume Improvement. Methods are enclosed in ellipses, while outputs are enclosed in rectangles.

2.2 Hypervolume Improvement

The concept of hypervolume improvement is illustrated in Figure 2. This figure represents a case with two objective functions, *F1* and *F2*, for which smaller values are assumed to indicate better performance.



a) Hypervolume of the Pareto front in the two-dimensional case.

b) Hypervolume corresponding to an arbitrary set of $F1_c^i$ and $F2_c^i$ values, indicated by a red diamond.



c) Probability density function assumed to follow a Gaussian distribution. The probability of the mean value of $F2_c$ is the highest, but $F2_c^i$ are still possible, albeit with lower probability.

d) Hypervolume improvement from an arbitrary point ($F1_c^i$ and $F2_c^i$), shown as a red diamond.

Fig. 2 Concept of Hypervolume Improvement.

In Figure 2a, the solid line represents the Pareto-optimal solutions (i.e., the Pareto front), on which an infinite number of such solutions exist. The reference point is defined by the limiting values of the Pareto-optimal solutions on the *F1* (horizontal) and *F2* (vertical) axes. The hatched purple area, bounded by the Pareto front and the reference point, represents the hypervolume in the two-dimensional case. When three objective functions are considered, the hypervolume becomes a volume in three-dimensional space. For four or more objectives, it is referred to as a hypervolume in higher-dimensional space.

In Figure 2b, the triangle represents the objective function values predicted by Gaussian Process Regression (GPR) for a given set of arbitrary design variables, $\boldsymbol{x}$. GPR provides both the predicted mean and the variance (i.e., uncertainty) for each objective function. It is important to note that the predicted mean values are not deterministic; rather, they represent the most probable values under the assumption of a Gaussian distribution. Importantly, there are many other potentially promising sets of objective function values—shown as red and black diamonds around the green triangle (which represents the predicted means) in Figure 2b—even if each has a low individual probability. Some of these sets outperform the current Pareto front. For instance, the red point dominates the current Pareto front, leading to the formation of a new Pareto front, shown as the solid red line in Figure 2b. This new Pareto front generates an updated hypervolume when combined with the reference point.

Figure 2c illustrates the Gaussian distribution associated with the objective function *F2* for a given set of design variables, $\boldsymbol{x}$. While the predicted mean value $F2_c$ corresponds to the highest probability under the Gaussian (bell-shaped) distribution, there remains a non-zero probability that the true value deviates from the mean. For instance, a value such as $F2_c^i$ indicated by a red diamond in Figure 2b, is possible. However, the likelihood of observing values significantly different from the mean decreases rapidly, in accordance with the properties of the Gaussian dist ribution, as shown in Figure 2c.

Figure 2d illustrates the definition of hypervolume improvement. The hypervolume associated with one of the promising sets—represented by the red diamond—is shown as the red hatched area. The difference between this red hatched area in Figure 2b and the purple area in Figure 2a corresponds to the hypervolume improvement.

It should also be noted that the red diamond is merely an example; thus, the hypervolume improvement shown in Figure 2d is illustrative. There are many other black diamonds (i.e., arbitrary points representing combinations of $F1_c^i$ and $F2_c^i$) around the predicted mean, as shown in Figure 2b. Each diamond has its own hypervolume improvement if it dominates the current Pareto front.

2.3 Expected Hypervolume Improvement (EHVI)

Figure 3 illustrates the concept of Expected Hypervolume Improvement (EHVI). On the right-hand side of the Pareto front, no improvement is possible; therefore, this region is excluded from consideration. In contrast, the left-hand side of the Pareto front is shown with a color gradient representing the probability distribution around the green triangle, which denotes the candidate solution. This distribution is assumed to follow a Gaussian (normal) distribution. The probability is expressed by the color gradation: darker colors indicate higher probability, whereas lighter colors indicate lower probability. The farther a point is from the candidate solution, the lower its probability becomes.

As shown in Figure 2b, each diamond-shaped point represents a possible outcome, and each outcome is associated with both a probability and a corresponding hypervolume improvement. The Expected Hypervolume Improvement is defined as the weighted sum of these hypervolume improvements, where each improvement is weighted by its associated probability.

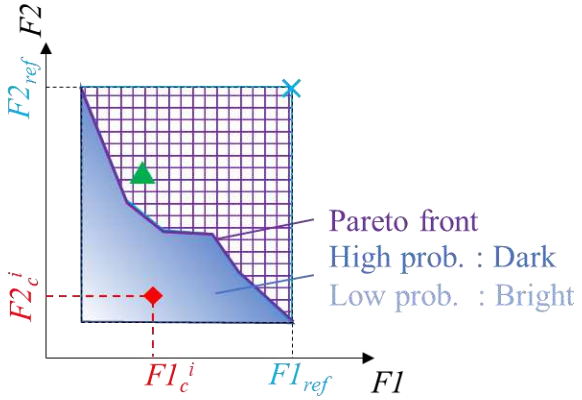


Fig. 3 Concept of Expected Hypervolume Improvement (EHVI).

The formal definition of EHVI is given in Eq. (1) for the two-dimensional case. When two objective functions are considered, Eq. (1) can be applied directly. In contrast, in the multi-objective case (i.e., the n-

dimensional case), the definition extends to an n-fold integral as defined by Eq. (2).

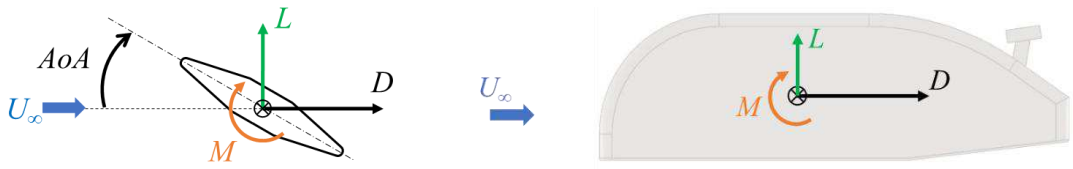
$$EHVI = \int_{-\infty}^{F1_{ref}} \int_{-\infty}^{F2_{ref}} HVI\big(F1(\vec{x}), F2(\vec{x})\big) \times \Phi_1\big(F1(\vec{x})\big)\Phi_2\big(F2(\vec{x})\big)\, dF1dF2 \tag{1}$$

$$EHVI = \int_{-\infty}^{F1_{ref}} \int_{-\infty}^{F2_{ref}} \cdots \int_{-\infty}^{Fn_{ref}} HVI \cdot \Phi_1\Phi_2 \cdots \Phi_n\, dF1dF2 \cdots dFn \tag{2}$$

Here, *HVI* denotes hypervolume improvement, and $\Phi_1(F1)$ denotes the corresponding probability density.

2.4 Definition of Aerodynamic forces and moment

Figure 4 illustrates the definitions of the aerodynamic forces and moment. The freestream velocity is denoted by U_∞. Drag (D) is defined along the direction of motion, lift (L) acts upward, and the pitching moment (M) is defined as positive when it induces a nose-up rotation about the center of gravity.



(a) Discus. (b) Race car (Ahmed body model) with a rear wing.

Fig. 4 Definition of Aerodynamic Forces.

For the discus (Figure 4a), the three aerodynamic coefficients, C_D, C_L and C_m, are the drag coefficient, lift coefficient, and pitching moment coefficient, respectively. The drag and lift coefficients are defined using the dynamic pressure and the discus planform area, while the pitching moment coefficient is additionally normalized by the discus diameter.

On the other hand, the Ahmed body model [6] equipped with a rear wing (Figure 4b) was employed as a race car model. The three aerodynamic coefficients are defined in the same manner. The reference area is the frontal projected area of the vehicle, the reference length is the vehicle length.

2.5 Computational Fluid Dynamics (CFD)

To evaluate C_D, C_L, and C_m in Step 6 of Figure 1, CFD was conducted.

For the men's discus, the same procedure as that used in our previous paper [1] was adopted. The CFD analysis was performed using ANSYS 2024 R1, including DesignModeler, Meshing, and Fluent. Fluent solved the three-dimensional RANS and continuity equations by the finite volume method, with the SST k-ω model for turbulence. A velocity inlet of 25 m/s and a pressure outlet were applied. The remaining boundaries were treated as slip walls, and the discus surface was modeled as a no-slip wall.

For the Ahmed body with a rear wing, OpenFOAM v2106 was used. Large eddy simulation was

employed with the Smagorinsky subgrid-scale model. The governing equations were discretized by the finite volume method, and a second-order central differencing scheme was used for the advection terms. The inlet velocity was set to 25 m/s, and a pressure outlet condition was applied at the outlet. The bottom boundary was treated as a moving wall at 25 m/s, while the other boundaries were treated as slip walls. A no-slip condition was imposed on the Ahmed body and rear wing surfaces.

Table 1 compares the experimental fluid dynamics (EFD) results from Ref. [7] with the present CFD results for the baseline Ahmed body without a rear wing. The differences between EFD and CFD were 0.020 for C_D, 0.001 for C_L, and 0.014 for C_m, respectively. These small differences indicate that the present CFD approach provides reasonable agreement with the experimental results.

Table 1 Comparison between the experimental and present CFD results

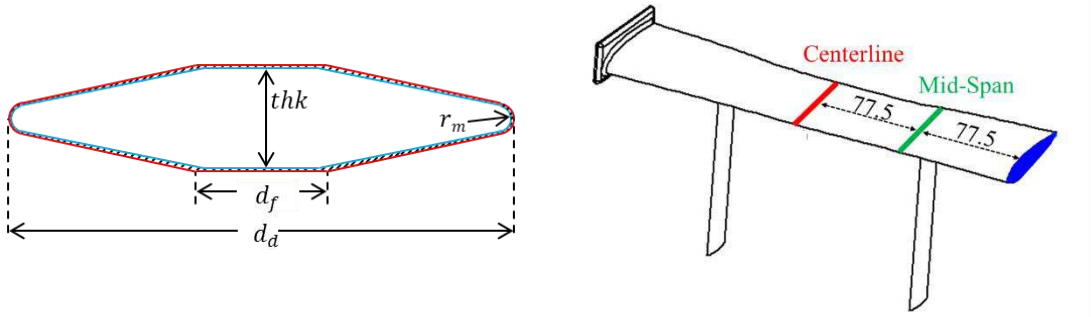
	C_D	C_L	C_m
EFD	0.244	-0.239	-0.151
CFD	0.224	-0.240	-0.165

2.6 Design variables

Figure 5 shows the design variables.

For the discus (Figure 5a), the definitions of four design variables are the same as those used in [1]. These are the discus diameter, d_d; the diameter of the flat center area, d_f; the thickness, thk; and the radius of the metal rim, r_m. Their allowable ranges under the regulations are 219-221 mm, 50-57 mm, 44-46 mm, and 5.85-6.45 mm, respectively.

For the rear wing, the airfoil shapes at the two cross sections shown as Centerline and Mid-Span in Figure 5b were used as design variables. Each airfoil shape was uniquely defined using the Joukowski transformation, with three design variables for each cross section. Thus, a total of six design variables were used for the rear wing. The wing-tip airfoil was fixed as NACA 0021. Each cross section was smoothly connected in the spanwise direction by spline curves. Winglets were attached at both ends of the wing as rectangular plates with dimensions of 30 mm in height, 80 mm in length, and 5 mm in width. All corners were filleted with a 2.5 mm radius. The total span of the rear wing, including the winglets, was set to 160 mm. Additionally, the angle of attack of the wing, defined as the angle between the wing chord and the direction of motion, was included as the seventh design variable. The allowable ranges of the chord length, maximum airfoil thickness, and angle of attack were 40-100 mm, 10-20 mm, and -20 to 20 degrees, respectively.



(a) Four design variables for the discus. The blue and red lines show the respective minimum and maximum size of the discus, as defined in the regulations.

(b) Seven design variables for the rear wing. Three design variables were assigned to each cross section, namely the centerline and mid-span sections, and the angle of attack was included as an additional design variable.

Fig. 5 Design variables for the discus and rear wing

2.7 Objective functions (Index of performance)

For the discus, the objective functions are flight distance and robustness [4], resulting in a two-objective optimization problem. Robustness is an index of the insensitivity of flight distance to variations in the design variables. A smaller robustness value is preferable because it indicates that the flight distance is less sensitive to changes in the design variables. Therefore, both objective functions, *F1*: negative flight distance and *F2*: robustness, should be minimized.

In contrast, for the race car rear wing, the objective functions are the drag coefficient, lift coefficient, and pitching moment coefficient, resulting in a three-objective optimization problem. All three objective functions, *F1*: C_D, *F2*: C_L, and *F3*: C_m, should be minimized. Note that a smaller value of C_L, that is, a more negative value of C_L, corresponds to a larger downforce.

2.8 Constraints

The only constraint for the discus is that it must land within the sector.

In contrast, two geometric constraints are imposed on the race car rear wing to ensure a smooth transition between the centerline and mid-span airfoil sections in the spanwise direction. The difference in chord length between the centerline and mid-span airfoil sections must be less than 30 mm, and the difference in maximum thickness between these sections must be less than 10 mm.

2.9 Optimization

The optimization was carried out using a genetic algorithm (GA) [8, 9].

For the men's discus, the eight release conditions [1] were optimized for flight distance and robustness in Step 8 of Figure 1, yielding the Pareto-optimal solutions. The release height is assumed to be 1.73 m, which is generally 90% of the thrower's height [10], and the release speed was assumed to be 24 m/s [11]. One release condition set was then selected as the solution farthest from the reference point shown

in Figure 2(a), thereby determining the optimal release conditions. In addition, the GA was applied in Step 13 of Figure 1 to optimize the acquisition function, i.e., the expected hypervolume improvement (EHVI). The design variable set that maximized the EHVI was adopted as the new promising design set, $\boldsymbol{x}^*$, shown in Step 15 of Figure 1.

For the rear wing, the EHVI was optimized in the same manner, and the resulting design variable set was adopted as the new promising design set, $\boldsymbol{x}^*$.

2.10 Test problem to confirm EHVI

As a benchmark to evaluate the effectiveness of EHVI, the welded-beam design problem [1] was employed. This problem considers a beam of height T and thickness B welded to a rigid support through a weld of length L and height H, while a concentrated load F is applied at the free end. The objective is to determine the design variables to minimize both the beam-tip displacement and the fabrication cost. These two objectives are inherently conflicting, since improving structural stiffness typically requires additional material, thereby increasing the manufacturing cost. The details are described in in the Online Resources.

This problem is widely used as a benchmark for constrained multi-objective optimization because it exhibits a clear trade-off between structural compliance and cost while involving both geometric and stress-related feasibility conditions.

3 Results

3.1 Test problem for evaluating EHVI performance

Figure 6 shows the objective space of the welded-beam design benchmark problem. The two objective functions and four design variables are listed in Tables S1.1 and S1.2 of the Online Resources. Both objective functions are normalized, and lower values are preferred for both objectives. The 20 initial samples generated by Latin hypercube sampling (LHS) are shown as open circles, while the 20 additional samples selected by EHVI are shown as crosses. The solutions selected by EHVI are in good agreement with the reference Pareto front obtained by NSGA-II. Of the 16 Pareto-optimal solutions, 13 were identified by EHVI, corresponding to 81% of the total. If EHVI were able to identify all Pareto-optimal solutions, its performance could be considered ideal. However, the diversity of the selected solutions is limited, as they are concentrated near the origin.

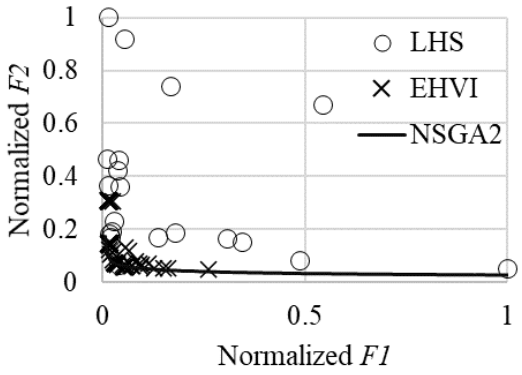


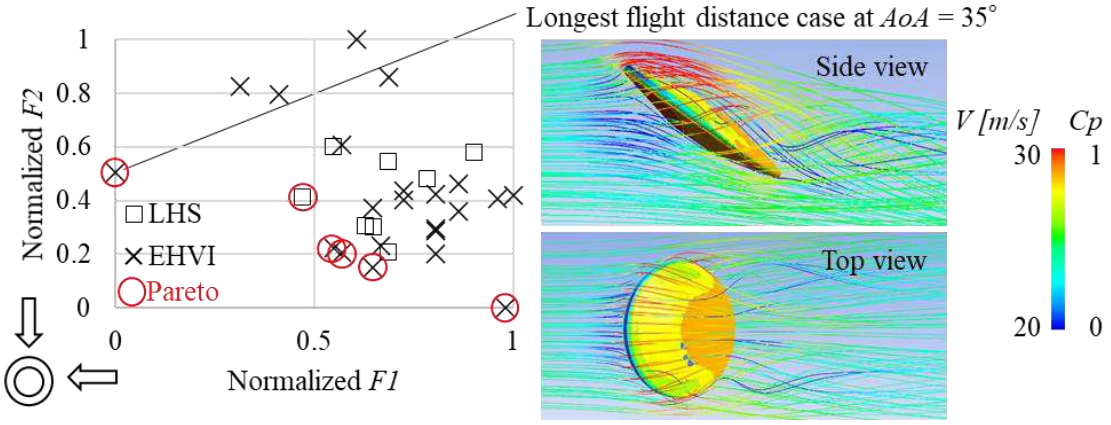
Fig. 6 Objective space for the test problem. Both objective functions are normalized by their respective maximum values. *F1* represents the beam-tip displacement, and *F2* represents the manufacturing cost. Open circles denote the initial samples generated by LHS, while crosses denote the additional samples selected by EHVI. The solid line represents the reference Pareto front obtained using NSGA-II [8].

3.2 Discus

The same Python code used for the benchmark problem was applied to the discus case, which likewise involves two objective functions and four design variables. Unlike the benchmark problem, however, this optimization required CFD analyses and a large number of trajectory simulations. In this study, 1000 Monte Carlo trajectory simulations were performed to estimate robustness in Steps 7 and 8 of Figure 1. As a result, the computational cost was high. Therefore, only eight initial samples were generated using Latin hypercube sampling (LHS), followed by 22 additional samples selected by EHVI.

Figure 7a shows the objective space of the discus case. Both objective functions are normalized, and lower values are preferred for both objectives. Of the six Pareto-optimal solutions, five were identified by EHVI, indicating that EHVI was effective in selecting promising additional design points in this case.

Figure 7b shows the streamlines and pressure distribution for one of the Pareto-optimal solutions, corresponding to the design with the longest flight distance at an angle of attack (*AoA*) of 35 degrees, viewed from the side and top. The streamlines and pressure distribution are colored by velocity magnitude and pressure coefficient, respectively. No boundary-layer separation is observed, suggesting that the discus maintains attached flow even at this relatively high angle of attack.

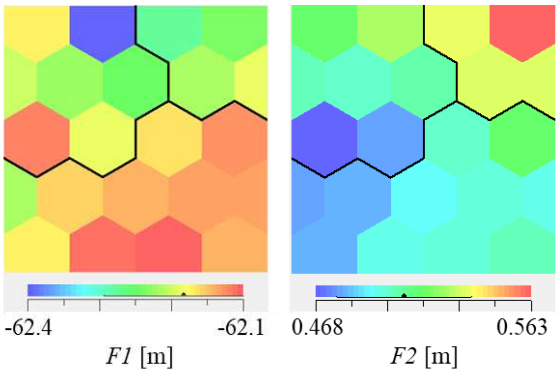


a) Objective space. Open circles represent the initial samples generated by LHS, while crosses represent the additional samples selected by EHVI. The red circles indicate the Pareto-optimal solutions.

b) Longest-flight-distance case at an *AoA* of 35 degrees. Streamlines and pressure distribution are colored by velocity magnitude and pressure coefficient, respectively.

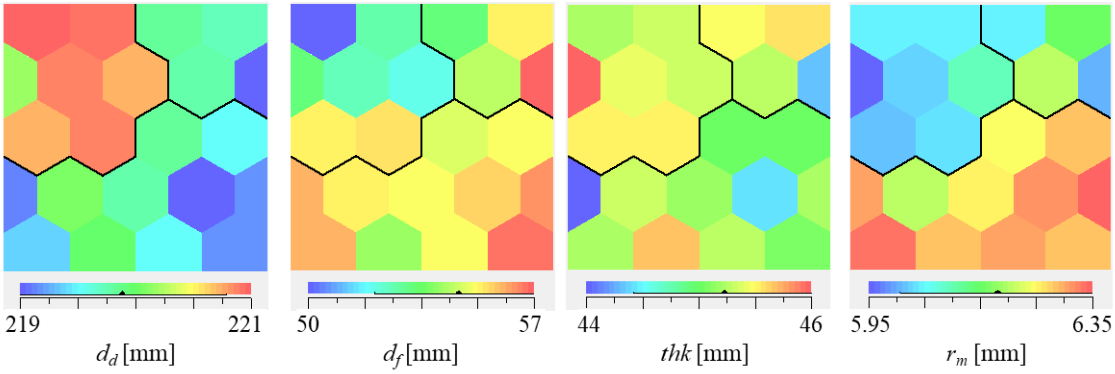
Fig. 7 Objective space and flow field for the discus.

The optimal aerodynamic design space of the discus was explored using the self-organizing maps [12] shown in Figure 8, following the method proposed in our previous paper [1]. The color pattern of *F1* (Figure 8a) varies mainly in the vertical direction, from the highest value (red) to the lowest value (blue). This pattern is similar to that of r_m (Figure 8f), indicating that *F1* is strongly influenced by the radius of the metal rim, r_m. In contrast, no design variable exhibits a color pattern clearly similar to that of *F2* (Figure 8b), suggesting that the dependence of robustness on the design variables is more complex.



a) Objective function, *F1*

b) Objective function, *F2*



c) Design variable, d_d d) Design variable, d_f e) Design variable, thk f) Design variable, r_m

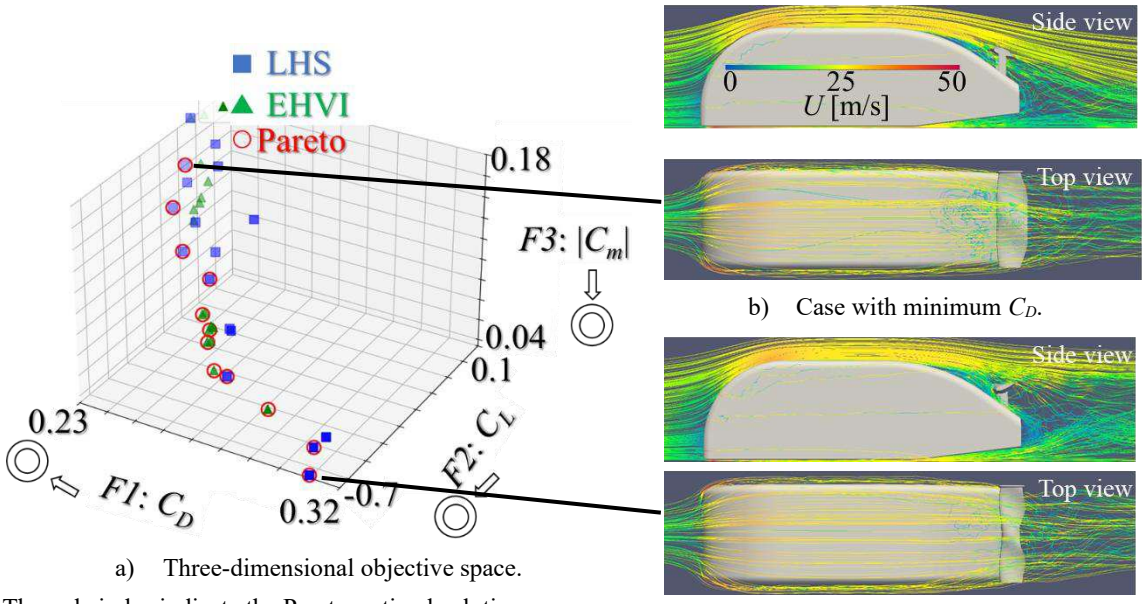
Fig. 8 Self-organizing maps for the objective functions and design variables. Exploration of the six-dimensional design space was carried out using self-organizing maps. Blue denotes the lowest value, while red denotes the highest value. Each hexagon represents a single sample point.

3.3 Race car rear wing

Figure 9a shows the three-dimensional objective space for the rear-wing case. In this case, the objective functions are defined as C_D, C_L, and $|C_m|$. Ideally, all three objective functions should be minimized simultaneously, corresponding to reduced drag, increased downforce (i.e., more negative lift), and reduced pitching motion.

The initial 17 samples generated by LHS are denoted by closed squares, while the additional 17 samples obtained using EHVI are denoted by closed triangles. The distribution of the solutions indicates that the three objective functions conflict with one another, exhibiting clear trade-offs among them. Of the 12 Pareto-optimal solutions, five were identified by EHVI, corresponding to 42% of the total.

Two extreme Pareto-optimal solutions are shown in Figures 9b and 9c. Figure 9b shows the case with the minimum C_D, whereas Figure 9c shows the case with the maximum downforce. The most notable difference between these two extreme cases is the angle of attack of the wing, as seen in the side views in Figures 9b and 9c. In the minimum-C_D case (Figure 9b), the wing inclination is nearly aligned with the rear-deck angle. In contrast, in the maximum-downforce case (Figure 9c), the wing is oriented at approximately 40 degrees relative to the rear-deck angle. The top views in Figures 9b and 9c further show that the wing area is relatively large in Figure 9b, whereas the wing becomes narrower around its center in Figure 9c.



a) Three-dimensional objective space. The red circles indicate the Pareto-optimal solutions.

b) Case with minimum C_D.

c) Case with minimum C_L (maximum downforce).

Fig. 9 Three-dimensional objective space for the rear-wing case and the corresponding flow fields.

4 Discussion

Promising design variables were identified using Expected Hypervolume Improvement (EHVI) in both case studies. However, the performance of EHVI differed between the discus and rear-wing cases.

In the discus case, the additional design points selected by EHVI accounted for 81% of the Pareto-optimal solutions, as shown in Figure 7a. In contrast, in the rear-wing case, the additional design points selected by EHVI accounted for only 42% of the Pareto-optimal solutions, as shown in Figure 9a. One possible reason for this difference is the dimensionality of the problem. The discus case involves two objective functions and four design variables, whereas the rear-wing case involves three objective functions and seven design variables. The rear-wing case therefore has a broader design and objective space to be explored, which may make it more difficult for EHVI to identify a wide range of Pareto-optimal solutions efficiently.

Furthermore, as illustrated in Figures 6 and 7a, the solutions selected by EHVI tend to be concentrated near the center of the objective space. Taken together, these observations suggest that the current EHVI-based approach may have limited ability to identify extreme Pareto-optimal solutions and, more generally, to ensure sufficient diversity among the selected solutions.

In the discus case, the radius of the metal rim appears to be the most influential design variable. As indicated by the self-organizing maps in Figure 8, the distribution pattern of *F1* is similar to that of r_m, suggesting a strong relationship between flight distance and the radius of the metal rim. This parameter may contribute to delaying flow separation, which triggers stall, and may therefore play an important role in improving aerodynamic performance.

In the rear-wing case, the angle of attack appears to be the most influential design variable. In the minimum-C_D case, the wing inclination is aligned with the rear-deck angle, as shown in Figure 9b. In contrast, in the maximum-downforce case, the wing inclination is oriented in the opposite direction relative to the rear-deck angle, as shown in Figure 9c, thereby increasing downforce. In addition to this difference in orientation, the wing geometry also differs between the two cases. The top views show that the maximum-downforce design becomes narrower around the centerline (Figure 9c), design has a larger effective wing area (Figure 9b). These results suggest that, in the maximum-downforce case, the wing orientation relative to the rear deck primarily contributes to increasing downforce, while a smaller wing area near the centerline may help reduce C_D and $|C_m|$. Conversely, in the minimum- C_D case, alignment of the wing with the rear deck primarily contributes to reducing C_D, while a larger wing area near the centerline may help maintain downforce.

5 Conclusions

Sports equipment design often involves multiple conflicting objective functions. This study proposed the use of Expected Hypervolume Improvement (EHVI) as a criterion for efficiently selecting design variables in multi-objective sports equipment optimization. A flowchart of the proposed framework was presented, and two aerodynamic case studies were conducted to demonstrate its applicability. The results showed that EHVI can identify Pareto-optimal solutions and key design variables in sports equipment design. However, the solutions selected by EHVI tended to cluster near the center of the objective space, suggesting limited ability to identify extreme Pareto-optimal solutions and to ensure sufficient diversity among the selected solutions.

Conflict of interest

Kazuya Seo serves on the Editorial Board of Sports Engineering. To avoid any potential conflict of interest, Kazuya Seo was not involved in the peer review or editorial decision-making process for this manuscript.

References

1. Seo, K., Kikuchi, R., Allen, T. (2025) Exploration of optimal aerodynamic design space for discus. Sports Eng 28, 28. https://doi.org/10.1007/s12283-025-00513-8
2. Shimoyama, K., Jeong, S., and Obayashi, S. (2012) Comparison of sample addition criteria for kriging response surface models in multi-objective optimization, Journal of Japanese Society for Evolutionary Computation (in Japanese), 3, 173-184, DOI: 10.11394/tjpnsec.3.173.
3. McKay, M.D., Beckman, R.J. and Conover, W.J. (1979) A comparison of three methods for selecting values of input variables in the analysis of output from a computer code, Technometrics, 21, 239–245, DOI:10.2307/1268522.

4. Seo, K., Shimoyama, K., Ohta, K., Ohgi Y., Kimura, Y. (2015) Optimization of flight distance and robustness in the discus. Sports Eng 18, 55–65. https://doi.org/10.1007/s12283-014-0166-y

5. Seo, K., Kobayashi, O. & Murakami, M. (2006) Multi-optimisation of the screw kick in rugby by using a genetic algorithm. Sports Eng 9, 87–96, DOI: 10.1007/BF02844861

6. Ahmed, S. R., Ramm, G., and Faltin, G. (1984) Some Salient Features of the Time-Averaged Ground Vehicle Wake, SAE Technical Paper 840300.

7. Nakajima T, Itoh Y, Sasa K, Ikeda M, Kato Y, Kitayama S, Kito K, Kori I, Koyama R, Shimada Y, Hanaoka Y, Higaki T, Fukuda K, Yamamura J, Li Y (2016) Wind tunnel tests of a simplified vehicle model for the validation of automotive aerodynamic CFD. Transactions of Society of Automotive Engineers of Japan 47(6):1439–1446. https://doi.org/10.11351/jsaeronbun.47.1439 (in Japanese)

8. Deb, K., Pratap, A., Agarwal, S. and Meyarivan, T. (2002) A fast and elitist multiobjective genetic algorithm: NSGA-II. IEEE Transactions on Evolutionary Computation. 6, 182-197, DOI: 10.1109/4235.996017

9. Sasaki, D., Obayashi, S. (2005) Efficient search for trade-offs by adaptive range multi-objective genetic algorithms. AIAA J Aerosp Comput Inf Commun 2:44–64.

10. Yamamoto, D., Murakami, M., Tsukada, T., Kato T., Takigawa, H. (2019) Characteristics of Tsutsumi's discus throwing motion: Comparison of 61.64m and 53.15m (in Japanese), Bulletin of Studies in Athletics of JAAF15, 261-264

11. Leigh, S., Liu, H., Hubbard, M. and Yu, B. (2010) Individualized optimal release angles in discus throwing, J Biomechanics, 43, 540-545.

12. Kohonen T (1995) Self-organizing maps. Springer, Berlin

Supplementary Files

This is a list of supplementary files associated with this preprint. Click to download.

- 260629OnlineResource.docx